Nano Research

Open Access

Research Article

Highly conductive sulfur iodide cathode accelerating sulfur redox kinetics for aqueous Zn–S batteries

Qianhui Zhang[1,§], Wenlin Zhang[1,§], Huan Wang[1], Chunhua Xu[1], Rui Li[1], Lin Xu[1], Xinyue Wang[1], Jihong Bian[2,3], Jianwei Wang[1] ✉, and Feng Fu[1]

[1] *School of Chemistry and Chemical Engineering, Yan'an University, Yan'an 716000, China*
[2] *Department of Physics, Shanghai Normal University, Shanghai 200234, China*
[3] *State Key Laboratory of ASIC and System, School of Microelectronics, Zhangjiang Fudan International Innovation Center, Fudan University, Shanghai 200433, China*
§ *Qianhui Zhang and Wenlin Zhang contributed equally to this work.*

Cite this article: *Nano Research*, **2026**, *19*, 94908050. https://doi.org/10.26599/NR.2025.94908050

ABSTRACT: Regarding the problems of low electrical conductivity and slow redox kinetics in Zn–S batteries, it is extremely urgent to find a simple and effective construction strategy. Herein, a conversion cathode material (S_xI, x = 9.3 and 1) was prepared by bonding commercial sulfur and iodine. Compared with commercial sulfur, the conductivity of S_xI is increased by 7 orders of magnitude. Density functional theory (DFT) calculated results show that new S–I chemical bonds are formed in S_xI materials, and the band gaps are significantly reduced. Their charge–discharge voltage differences, the differential capacity curves, and the redox peak potential difference of sulfur are significantly reduced. In the voltage window of 1.20–1.40 V, the I^0/I^- reversible redox reaction can provide additional capacity contribution of 38.36 mAh·g^{-1}. At the current density of 1.5 A·g^{-1}, the capacity of $S_{9.3}I$ could reach up to 370.32 mAh·g^{-1}, and SI could reach up to 220.04 mAh·g^{-1}. S_xI materials have a lower degree of polarization, a smaller Tafel slope, and activation energies. The *in-situ* ultraviolet–visible spectroscopy results indicate that the dissociation of the Zn–S bond during the charging process is mainly due to the interaction between I^- and the ZnS surface, promoting the rapid conversion of I_3^- to I^-. This work presents a paradigm for effectively enhancing the conductivity of sulfur cathode materials, increasing additional capacity and catalyzing sulfur conversion reactions, thereby significantly improving the performance of Zn–S batteries.

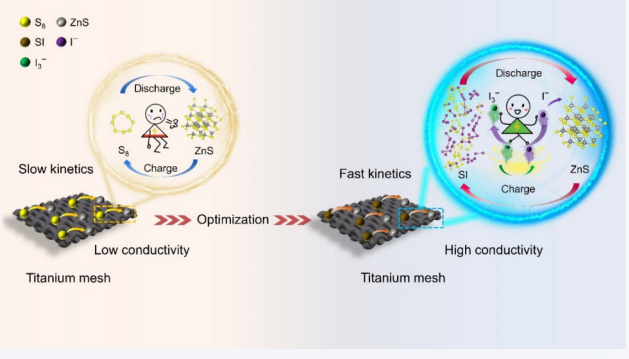

KEYWORDS: cathode material, redox reaction, electrical conductivity, catalytic activity, Zn–S batteries

1 Introduction

In order to cope with energy shortages and environmental crises, the development of green, non-flammable, and safe high-energy-density storage devices is imperative. Compared to non-aqueous electrolytes (10^{-3}–10^{-2} S·cm^{-1}), aqueous electrolytes have higher ionic conductivity (10^{-1}–6 S·cm^{-1}) [1, 2]. Zinc (Zn) metal, as the anode material, is more commonly used in the field of aqueous zinc ion batteries due to its advantages, such as high theoretical capacity (820 mAh·g^{-1}), good electrical conductivity (5.91 μΩ·cm), low electrochemical potential (–0.762 V vs. standard hydrogen electrode (SHE)), low environmental hazard, non-toxicity, and low price [3–6].

Currently, a larger number of intercalation-type cathode materials, such as manganese-based [7], vanadium-based [8], and Prussian blue analogues [9], have been widely used. However, due to the strong electrostatic interaction, their capacity (50–300 mAh·g^{-1}) and energy density are unsatisfactory [10, 11]. Facing these problems, researchers have discovered a series of cathode materials with conversion mechanisms, mainly including metal fluoride/sulfide/oxide, halogen materials, and sulfur (S)-based materials [12, 13]. Among them, sulfur-based materials can achieve a high energy density of more than 300 Wh·kg^{-1} in battery applications through multi-electron transfer redox reactions [14, 15]. However, there are mainly two aspects of problems that restrict its further development. On one hand, extremely low

Received: July 13, 2025; **Revised:** August 19, 2025
Accepted: September 8, 2025

✉Address correspondence to wangjianwei@yau.edu.cn

electronic conductivity. Elemental sulfur (S_8) and its discharge products (ZnS) are approximately 10^{-30} S·cm^{-1}, resulting in low utilization of active materials and discharge voltage plateau. On the other hand, slow kinetic processes. The kinetics of the solid–liquid–solid conversion reaction between sulfur and ZnS is slow, leading to high polarization voltage and low energy efficiency.

To address the issue of low conductivity, researchers have introduced carbon materials to construct sulfur-based carbon composite cathode materials. Sharma and co-workers constructed a biomass-derived porous carbon sulfur composite cathode material with a capacity retention rate of 47.6% after 200 cycles at a current density of 1 A·g^{-1} [16]. Meanwhile, our group found that three-dimensional porous amorphous carbon derived from asphalt has high conductivity (15.59 S·m^{-1}) and a large specific surface area (614.9 m^2·g^{-1}) [17]. The cathode material, by encapsulating industrial-grade sulfur, exhibits high reversible specific capacity (633.5 mAh·g^{-1}) [18]. In response to the slow conversion reaction, catalysts are introduced to enhance the redox kinetics of sulfur. Zhang et al. constructed incorporation of Fe–N_4 coordinated bi-directional catalytic sites of iron atoms in nitrogen-doped porous carbon skeletons as cathode for zinc–sulfur battery applications [19], which reached 519 mAh·g^{-1} at 0.5 A·g^{-1}. However, carbon materials and catalysts will increase the weight of cathode materials, and reduce the content of active sulfur, but make almost no contribution to the capacity of battery. Adding iodine (I) to the electrolyte has been proposed to accelerate the redox reaction of sulfur cathode [20]. Li et al. added 0.05 wt.% of I_2 to 1 M $Zn(CH_3COO)_2$, utilizing I_2 as an ion carrier for Zn^{2+} which can quickly achieve solid–liquid–solid conversion [21]. Mehta et al. discovered the catalytic role of I_2 in the conversion between S and ZnS by adding ethylene glycol and I_2 to $Zn(CH_3COO)_2$ [22]. In addition, iodine can serve as a cathode material to provide capacity in zinc iodine batteries [23, 24].

Inspired by these fascinating results, the introduction of iodine atoms into sulfur cathode materials could be a facile and effective strategy to settle multiple challenges for Zn–S batteries. Herein, a conversion cathode material (S_xI, x = 9.3 and 1) was prepared by bonding commercial sulfur and iodine. Compared to commercial sulfur, the conductivity of S_xI cathode material has increased by seven orders of magnitude, as iodine effectively breaks the S_8 ring and forms S–I bonds. The experimental results show that iodine plays a dual role in the sulfur conversion process: (1) The I^0/I^- reversible redox reaction can provide additional capacity contribution of 38.36 mAh·g^{-1} in the voltage window of 1.20–1.40 V. At the current density of 1.5 A·g^{-1}, the capacity of $S_{9.3}I$ can reach up to 370.32 mAh·g^{-1} and SI can reach up to 220.04 mAh·g^{-1}. (2) Accelerate the conversion reaction of sulfur species from both kinetic and thermodynamic perspectives. Compared with commercial sulfur, S_xI has a lower degree of polarization and a smaller Tafel slope. The activation energies of $S_{9.3}I$ and SI are 31.87 and 28.48 kJ·mol^{-1}, respectively, which are significantly lower than the activation energy (E_a) of sulfur at 47.69 kJ·mol^{-1}. *In-situ* ultraviolet–visible spectroscopy shows that during the charging and discharging process of the battery, some iodine undergoes a conversion reaction between I^0 and I^-, thereby catalyzing the solid–liquid–solid conversion of sulfur. The scanning electron microscopy (SEM) image of the S_xI material after cycling shows that another part of iodine remains in the material and can undergo I^0/I^- conversion on the electrode surface, directly achieving the solid–solid conversion of sulfur. This work presents a paradigm for effectively enhancing the conductivity of sulfur cathode materials, increasing additional capacity and catalyzing sulfur conversion reactions, thereby significantly improving the performance of Zn–S batteries.

2 Experimental

2.1 Materials

The chemicals and materials were all commercially available products and were used directly without further purification. Industrial sulfur powder originated from Shaanxi Yanchang Petroleum (Group) Co, Ltd. (China), and iodine was purchased from Macklin. For the experimental setup, we employed Zn foil with a thickness of 50 μm as anode, glass microfiber filter (Whatman GF/D), and a titanium mesh with a mesh size of 200. Deionized water used in all experiments was purified through a Millipore system (18.25 MΩ·cm).

2.2 Synthesis of S_xI

At room temperature, 0.7 g of sulfur powder and 0.3 g of iodine were ground at a stoichiometric ratio of 9.3:1 until the color was uniform. The reactants were transferred to a 50 mL stainless steel autoclave lined with Teflon and heated at a rate of 1 °C·min^{-1} to 80 °C for 3 h. The final product was named $S_{9.3}I$. Using a similar method, the stoichiometry ratio of sulfur and iodine was adjusted to 1:1, by employing 0.2 g of sulfur and 0.8 g of iodine to obtain the final product named SI.

2.3 Structural characterizations

The morphology and microstructure of the samples were observed by field emission SEM (MIRA4 LMH) with an energy dispersive spectrometer (EDS, Ultim Max 40). X-ray diffraction (XRD) patterns were collected using a Bruker D8 Advance diffractometer (Cu Kα, λ = 1.5418 Å, Germany) at 40 kV and 40 mA, at a 2θ range of 10°–80° and a scan rate of 10 °·min^{-1}. The Raman spectra were obtained by InVia Qontor (λ = 785 nm, UK). The samples were measured on a TA 250 differential scanning calorimetry (DSC) protected by a nitrogen atmosphere with a temperature increase rate of 5 °C·min^{-1} and a temperature increase range of 30 to 150 °C.

2.4 Electrical conductivity measurement

The powder samples were pressed into 5 mm diameter discs and tested with a four-probe direct current (DC) resistance tester (Tonghui TH2515), in which an insulation resistance tester was used to test insulating samples. The samples were placed between two pieces of copper foil, and four silver wires were attached to the copper foil as probes for the four-point probe resistance measurement. The equation for calculating conductivity (σ) is $\sigma = L/(RS)$, where R is the test resistance, S is the cross-sectional area of the sample, and L is the distance between the two probes.

2.5 Preparation of the disk electrodes

N-methyl-2-pyrrolidone (NMP) was used as the solvent; the active material, Super P, and polyvinylidene difluoride (PVDF) were mixed well at the ratio of 7:2:1. The slurry was coated on a titanium mesh, which was dried at 60 °C for 12 h in a vacuum drying oven. The titanium mesh was cut into disc electrodes with a diameter of 12 mm. The obtained disc electrode was used as the cathode, the glass fiber was used as the separator, the zinc foil was used as the

anode, and the CR2032 battery was assembled in air, in which the electrolyte solution was 1 M $Zn(OAc)_2$, where OAc was acetate. The active material loading was 1–2 mg·cm^{-2}.

2.6 Electrochemical measurements

Cycling and rate performance were tested by a battery test system (CT2001A, Rand Corporation, Wuhan, China) with a voltage range of 0.1–1.6 V. The cyclic voltammetry (CV) and electrochemical impedance spectroscopy (EIS) measurements were performed by a CHI 660E electrochemical workstation (Shanghai Chenhua, China). The ultraviolet–visible (UV–vis) spectra were obtained on the UV-2550 spectrophotometer. In the *in-situ* UV–vis tests, $S_{9.3}I$ material was first selected the open circuit voltage of 1.38 V. Subsequently, charging was performed in 0.1 V increments from 1.4 V up to 1.6 V, followed by discharging in 0.1 V increments down to 0.1 V, and finally charging again in 0.1 V increments up to 1.6 V. During the test, each voltage was maintained for 300 s to facilitate real-time monitoring and observation of the iodine conversion process. SI material was first selected at 1.41 V for UV–vis testing; other testing steps followed the same steps as described above.

2.7 Computational details

All the calculations in this study were performed by density functional theory (DFT) and implemented using the Vienna *ab initio* simulation package (VASP). The electron–ion interactions were treated using the projection enhanced wave (PAW) pseudopotentials. The Perdew–Burke–Emzerhof (PBE) and generalized gradient approximation (GGA) functions were adopted to describe the exchange-correlation effects. The plane wave cutoff was set to be 450 eV, and the Brillouin zone sampling was calculated using a 3 × 3 × 2 grid of *K*-points. After optimization of the structure, the energy converged to 10^{-6} eV per atom and the force converged to 0.02 eV·Å^{-1}.

3 Results and discussion

S_xI was characterized by XRD measurement, and both (x = 9.3 and 1) showed the characteristic peaks of the sulfur phase (Fig. 1(a)). Compared with the characteristic peaks of commercial sulfur, the peaks of $S_{9.3}$I shifted to 23.20°, 25.96°, and 27.89°, and the peaks of SI shifted to 23.22°, 25.98°, and 27.85°, corresponding to the (222), (026), and (206) crystal planes, respectively (Fig. 1(b)). With the

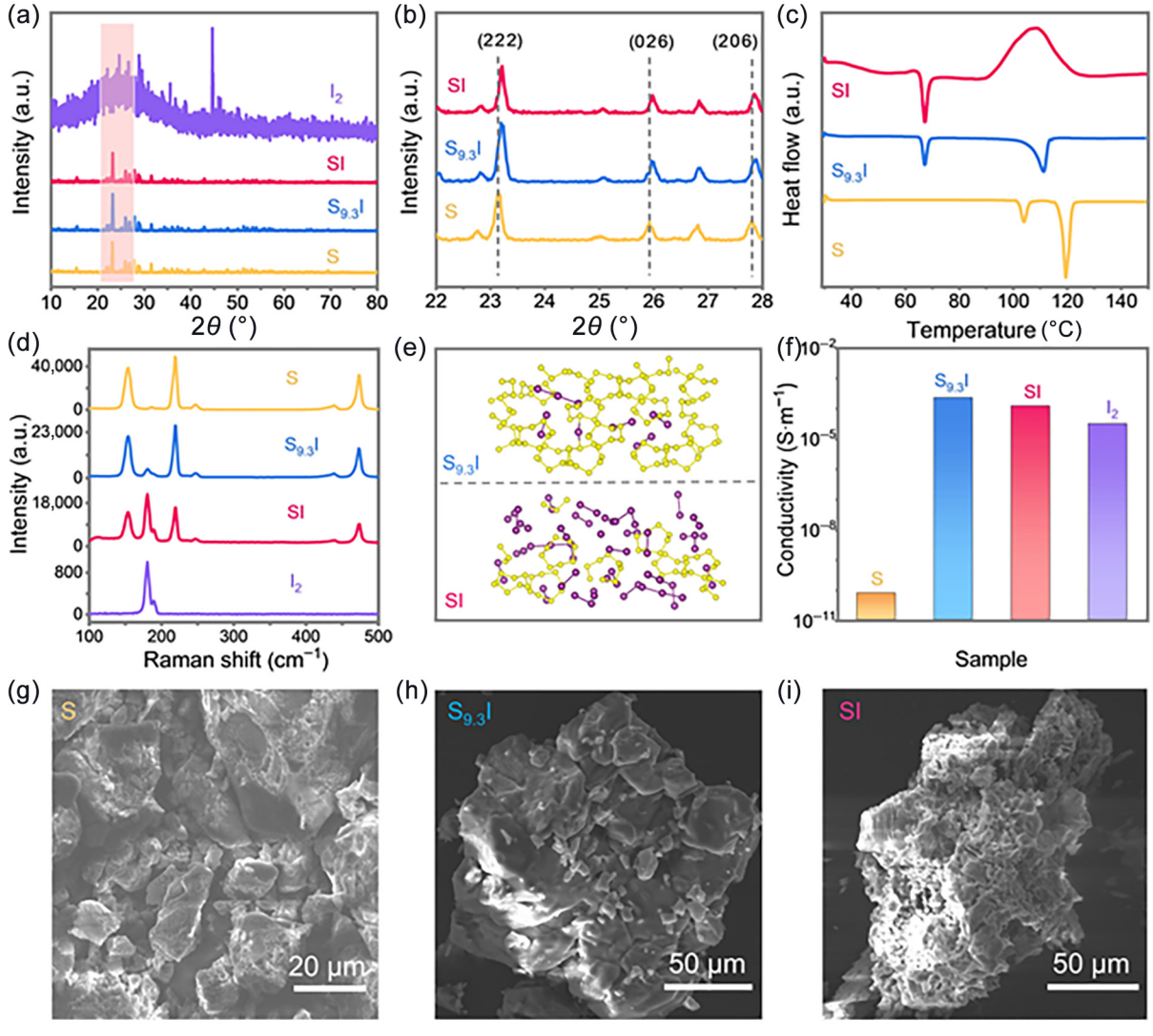

Figure 1 Structural and morphological characterization. (a) XRD patterns. (b) Local magnifications of XRD. (c) DSC curves. (d) Raman spectra. (e) The optimized molecular structures. (f) Electric conductivity. ((g)–(i)) SEM images.

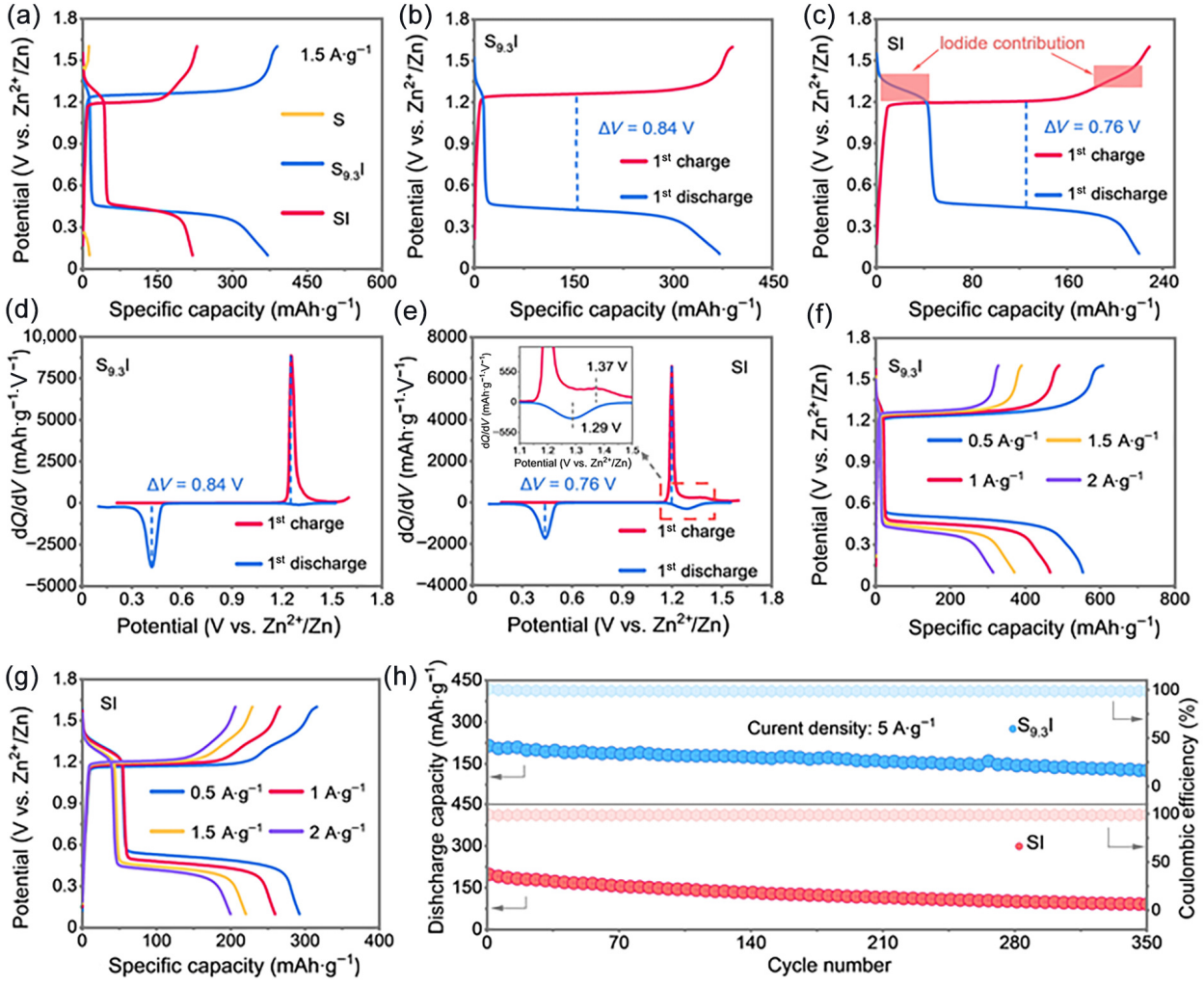

Figure 2 Electrochemical performance. (a) GCD profiles at 1.5 A·g^{-1}. ((b) and (c)) The initial GCD profiles of $S_{9.3}I$ and SI at 1.5 A·g^{-1}. ((d) and (e)) The differential capacity (dQ/dV) plots of charge–discharge curves. ((f) and (g)) GCD curves of S_xI at different current densities. (h) Cycling performance of S_xI at 5 A·g^{-1}.

increase of iodine content, the peak of S_xI shifts to a higher angle. The results show that the lattice spacing of sulfur decreases, suggesting a strong bonding interaction between the iodine and sulfur phases. The thermal properties and phase transition behavior of these materials were analyzed by DSC, as shown in Fig. 1(c). The melting curve of commercial sulfur shows two distinct endothermic peaks, indicating that the crystal structure and intermolecular interactions of sulfur have changed. At 104.25 °C, the endothermic peak is the transformation of orthorhombic sulfur (α-S) to monoclinic sulfur (β-S), and the sulfur molecules are rearranged in the lattice. At the endothermic peak of 119.58 °C, β-S reaches its melting point and undergoes a transformation process from solid to liquid [25, 26]. When iodine is introduced to form S_xI materials, the endothermic peaks at 67.47 and 110.81 °C of $S_{9.3}I$ material represent the process of the melting change of the material. However, SI material firstly shows glass transition accompanied by enthalpy relaxation, then an endothermic peak appears at 67.47 °C and an exothermic peak at 108.79 °C for the solidification cross-linking of iodine. These results further prove the existence of a strong chemical bonding interaction between iodine and sulfur in S_xI materials.

The Raman results (Fig. 1(d)) present that both $S_{9.3}I$ and SI exhibit characteristic peaks of sulfur at 154.04 and 218.52 cm^{-1}, but the intensity of the characteristic peaks is significantly weakened compared with that of commercial sulfur. The characteristic peaks of iodine were displayed at 180.45 and 189.67 cm^{-1}, and the intensity of the characteristic peaks was the greatest in SI. These may result from the bonding interaction between iodine and sulfur [27]. The interaction between iodine and sulfur was elucidated by DFT calculations. The optimized molecular structures of $S_{9.3}I$ and SI are shown in Fig. 1(e). A large number of iodine molecules are intercalated between sulfur rings, and some iodine and sulfur form chemical bonds. The calculated results suggest that the S–S bond length is 2.06 Å, the I–I bond length is 2.89 Å, and new S–I chemical bonds are formed in $S_{9.3}I$ and SI materials with bond lengths of 2.64 and 2.58 Å, respectively.

Next, the electrical conductivity of S_xI material was measured by the four-point probe resistance to explore the influence of iodine atoms on the electronic structure of sulfur (Fig. 1(f)). Compared with the conductivity of commercial sulfur (7.59×10^{-11} S·m^{-1}), the conductivities of $S_{9.3}I$ and SI were 2.27×10^{-4} and 1.22×10^{-4} S·m^{-1}, respectively, which increased by 7 orders of magnitude. These results are attributed to the introduction of a semiconductor bandgap structure by iodine atoms in the S_8 ring (I_2, 3.13×10^{-5} S·m^{-1}), which alters the insulating property of sulfur itself and enhances the electron migration rate [28]. As shown

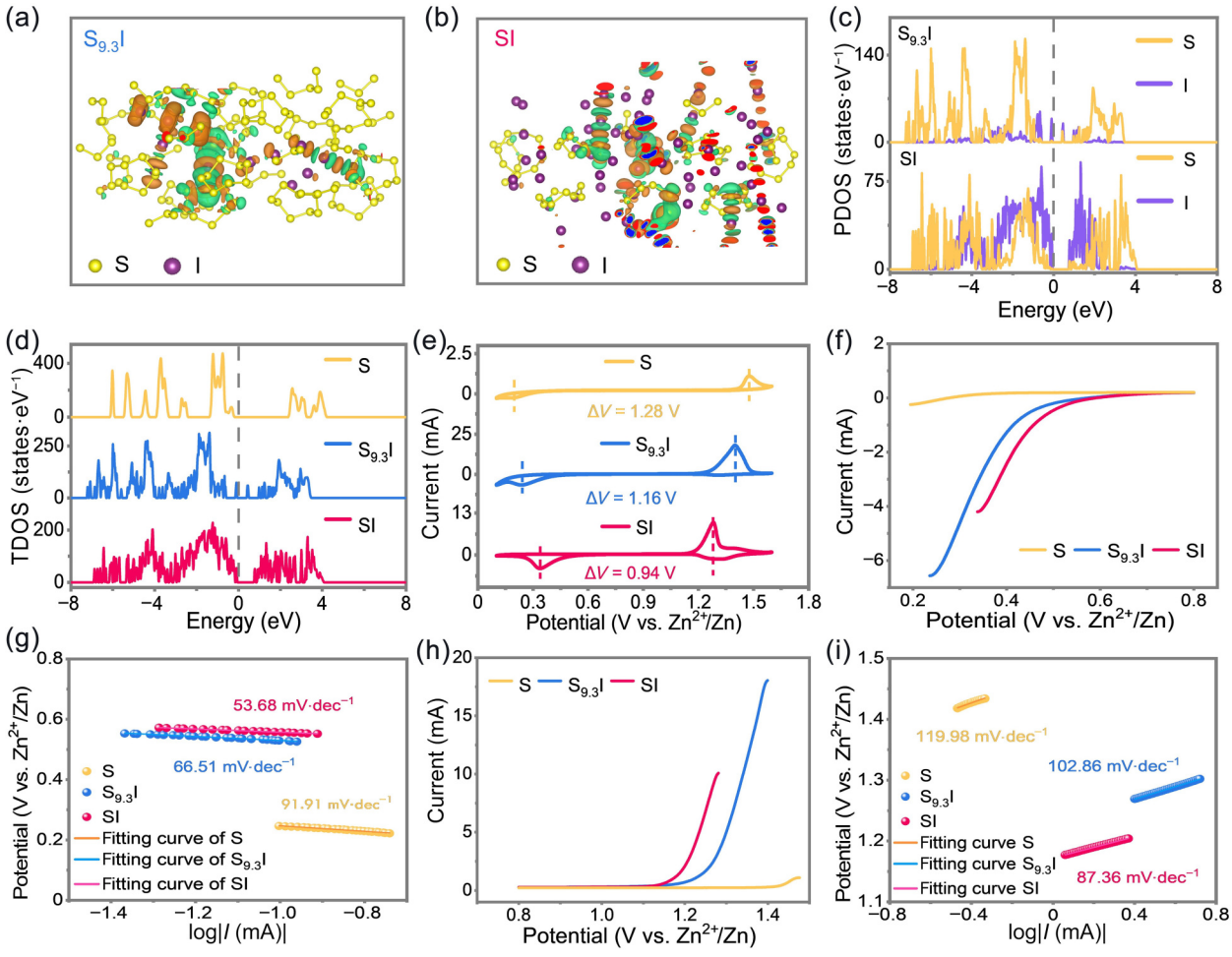

Figure 3 ((a) and (b)) Charge density distribution. (c) PDOS patterns. (d) TDOS patterns. (e) CV curves. (f) LSV curves for the reduction processes. (g) The corresponding Tafel slopes. (h) LSV curves for the oxidation processes. (i) The corresponding Tafel slopes.

in Figs. 1(g)–1(i), all three materials exhibit an irregular block-like morphology. Compared with commercial sulfur and $S_{9.3}I$ material (Fig. S1 in the Electronic Supplementary Material (ESM)), the surface of SI material with high iodine content has a rougher surface and abundant pores of various sizes. The energy-dispersive spectroscopy (EDS) mapping results (Fig. S2 in the ESM) demonstrated that S and I elements were uniformly distributed in the S_xI material.

In order to evaluate the electrochemical performance of S_xI materials, Zn–S batteries were assembled with 1 M $Zn(OAc)_2$ as the electrolyte. Compared with the extremely low initial discharge capacity of commercial sulfur material, the $S_{9.3}I$ and SI materials exhibit high discharge capacities of 370.32 and 220.04 mAh·g^{-1}, respectively, at a current density of 1.5 A·g^{-1} (Fig. 2(a)). Their charge–discharge voltage differences are significantly reduced, being 0.84 and 0.76 V, respectively (Figs. 2(b) and 2(c)). In the SI material with high iodine content, a reversible redox conversion reaction of I^0/I^- was clearly observed [29, 30], providing a discharge capacity of 38.36 mAh·g^{-1} in the high voltage range of 1.20–1.40 V. The differential capacity curves also clearly show that the redox peaks corresponding to the charge and discharge plateaus of the $S_{9.3}I$ and SI materials are 0.42/1.26 V and 0.43/1.19 V, respectively, as shown in Figs. 2(d) and 2(e). Significantly, the SI material shows a pair of redox peaks at 1.29/1.37 V, corresponding to the redox reaction of I^0/I^-, which is consistent with the result of the galvanostatic charge–discharge (GCD) curves in Fig. 2(c). Then, the overall electrochemical performance of S_xI was evaluated through the rate performance and cycling stability. As shown in Figs. 2(f) and 2(g), at current densities of 0.5, 1, 1.5, and 2 A·g^{-1}, the capacity of $S_{9.3}I$ material can reach 553.27, 465.85, 370.32, and 313.64 mAh·g^{-1}, and the SI material can reach 292.27, 259.37, 220.04, and 199.45 mAh·g^{-1}, respectively. For SI materials, the discharge capacities provided by the I^0/I^- redox couple at different current densities are 48.03, 47.77, 38.36, and 35.55 mAh·g^{-1}, respectively (Fig. S3 in the ESM).

To evaluate the stability of long cycles, the voltage differences of the charge–discharge curves of $S_{9.3}I$ and SI materials at the 10th, 30th, 50th, and 100th cycles were conducted (Fig. S4 in the ESM). After 350 cycles, the discharge capacity of SI reached 91.10 mAh·g^{-1}, while $S_{9.3}I$ remained at 126.30 mAh·g^{-1} at a high current density of 5 A·g^{-1} (Fig. 2(h)). In addition, compared to reported sulfur-based cathode materials (Table S1 in the ESM), S_xI material exhibits excellent cycling stability. It is mainly attributed to the introduction of iodine into the sulfur cathode material to form S_xI material, which accelerates electron transfer. The iodide ions formed in the redox reaction act as the medium, reducing the energy barrier required for the reaction, improving the voltage lag of Zn–S batteries, and promoting the reversibility of the changes at the zinc deposition/dissolution interface [31, 32].

The electron variation between sulfur and iodine atoms in S_xI

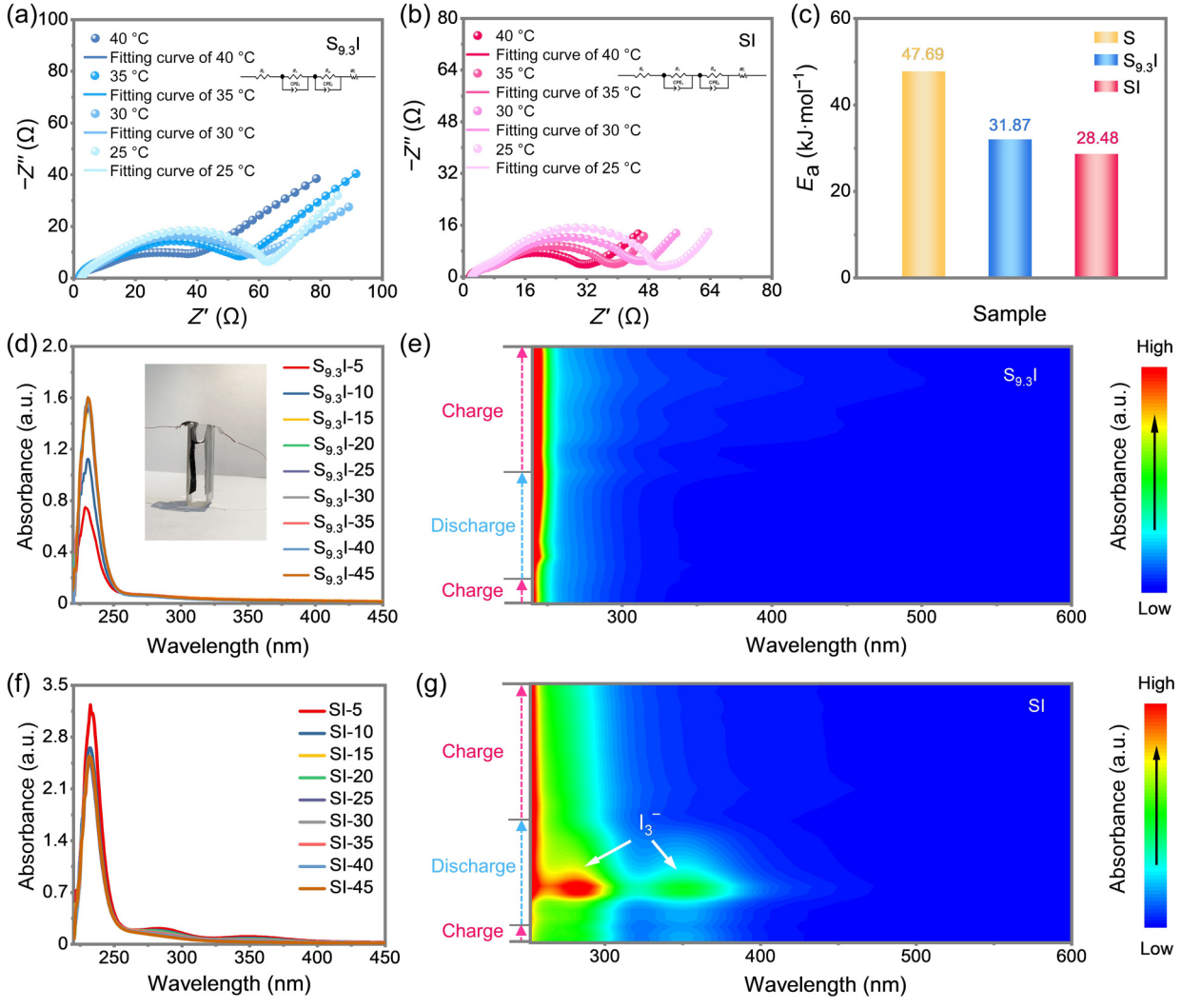

Figure 4 ((a) and (b)) EIS spectra of the Zn–S batteries at different temperatures in (a) $S_{9.3}I$ and (b) SI. (c) Comparison of the activation energies of S and S_xI. ((d) and (f)) The UV–vis spectra of $S_{9.3}I$ and SI after 5–45 cycles. ((e) and (g)) *In-situ* UV–vis spectra of $S_{9.3}I$ and SI.

materials was further revealed by the differential charge density distribution (Figs. 3(a) and 3(b)). The yellow and purple spheres represent S and I atoms. The orange region represents electron accumulation, and the green region indicates electron dissipation. When new S–I bonds are formed, the electrons around sulfur are exhausted while the electrons around iodine accumulate, indicating a close electron transfer between sulfur and iodine. Combined with the Bader charge results, it was found that the overall average loss of sulfur atoms in $S_{9.3}I$ was $0.005e^-$, while the overall average loss of sulfur atoms in SI was $0.010e^-$. The partial density of states (PDOS) and total DOS (TDOS) enable the analysis of the contribution of atoms and reflect the conductivity of these materials (Figs. 3(c) and 3(d)). Near the Fermi energy level, iodine in S_xI exhibits a higher DOS contribution than commercial sulfur, suggesting the introduction of iodine accelerates electron transport [33]. Furthermore, due to the p–p orbital coupling between sulfur and iodine in S_xI, the strength of S–I bond is increased (Fig. S5 in the ESM) [34, 35]. Notably, compared to the bandgap of 2.68 eV for commercial sulfur, the band gaps of $S_{9.3}I$ and SI are significantly reduced to 0.51 and 0.86 eV, respectively. Electrons are more likely to transition from the valence band to the conduction band [36], thereby enhancing the electrical conductivity of S_xI materials, which is consistent with the results of the electrical conductivity test.

To evaluate the redox kinetics of the three materials, their CV curves were tested at a scanning rate of 0.5 $mV·s^{-1}$ within the voltage range of 0.1 to 1.6 V (Fig. 3(e)). Sulfur exhibited a pair of distinct redox peaks corresponding to the reduction of S_8 and oxidation of ZnS. Compared with the redox peak potential difference of commercial sulfur (1.28 V), the polarization degrees of $S_{9.3}I$ and SI were significantly reduced to 1.16 and 0.94 V, respectively, indicating that iodine contributes to the catalytic conversion process of sulfur and accelerates the kinetics of reversible redox reactions. The SI material has a pair of redox peaks at 1.32/1.38 V, corresponding to the redox of I^0/I^-. Then, I^- can interact with the surface of ZnS to dissociate the Zn–S bond, and some I^- may also be converted into I_3^-, improving the reversibility of cycle [29, 37]. To reveal the catalytic effect of iodine, the Tafel slopes of the redox reactions were calculated by linear scanning voltammetry (LSV) curves, respectively (Figs. 3(f) and 3(h)). According to the reduction polarization curves, the Tafel slopes of S, $S_{9.3}I$, and SI were calculated to be 91.91, 66.51, and 53.68 $mV·dec^{-1}$, and the Tafel slopes obtained from the oxidation polarization curves were 119.98, 102.86, and 87.36 $mV·dec^{-1}$, respectively (Figs. 3(g) and 3(i)). S_xI shows a relatively low Tafel slope value in the redox reaction, indicating that iodine can

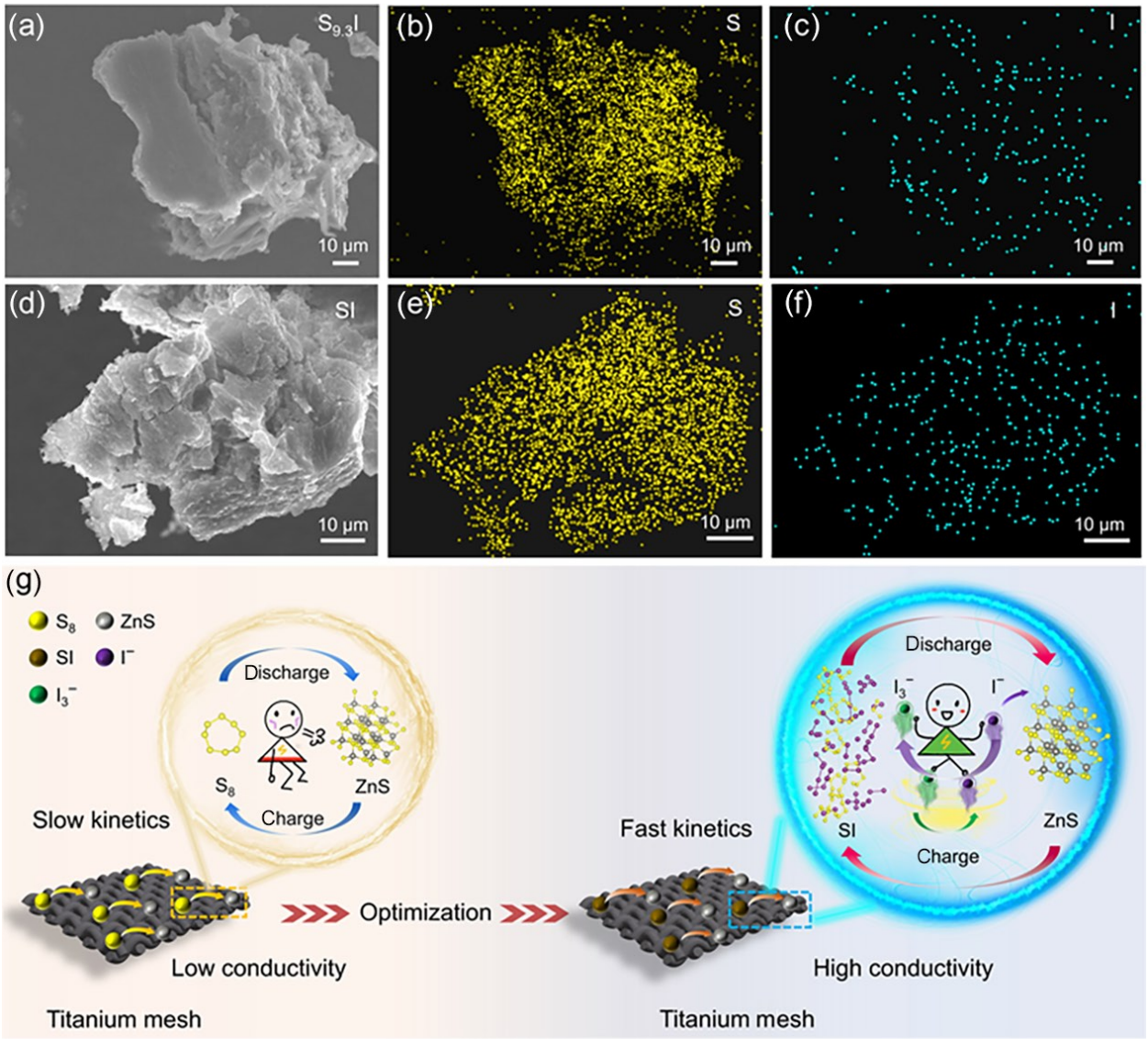

Figure 5 ((a)–(f)) SEM images of S_xI after charge and discharge processes. (g) Schematic illustration of S_xI cathode materials.

accelerate the transport of Zn^{2+} and promote the activation of ZnS, exhibiting high catalytic activity.

Variable-temperature EIS measurement was used to analyze thermodynamic processes. Figures 4(a) and 4(b) show the Nyquist diagrams and the corresponding equivalent circuit diagrams of S_xI at 25, 30, 35, and 40 °C. They present a distinct semi-circle in the high-frequency region and a diagonal line in the low-frequency region, indicating that both charge transfer and ion diffusion exist in the electrochemical reaction process. Compared to the charge transfer resistance of commercial sulfur at different temperatures (Fig. S6 in the ESM), $S_{9.3}I$ has a smaller resistance value, while SI has the smallest resistance value, as shown in Table S2 in the ESM. The E_a calculated by the Arrhenius equation shows that the activation energy of commercial sulfur is 47.69 kJ·mol^{-1}, while the activation energies of $S_{9.3}I$ and SI significantly decrease to 31.87 and 28.48 kJ·mol^{-1}, indicating that iodine reduces the energy barrier of the conversion reaction and improves the catalytic efficiency (Fig. 4(c)). The catalytic conversion mechanism of iodine in different cycle numbers was investigated by UV–vis spectroscopy (Figs. 4(d) and 4(f)). The $S_{9.3}I$ material shows an I^- absorption peak at ~ 231 nm. At the beginning, with the increase of the number of cycles, the concentration of I^- gradually increases until I^- and I^0 reach equilibrium after 15 cycles [38]. In addition to showing the absorption peak of I^-, the SI material also exhibits the absorption peak of I_3^- at 280 and 350 nm [39, 40]. With the increase of the number of cycles, the absorption peak intensities of I^- and I_3^- gradually weaken and eventually reach equilibrium. The mechanism of iodine during the charging and discharging process was further analyzed by *in-situ* UV–vis spectroscopy (Figs. 4(e) and 4(g) and Fig. S7 in the ESM). During the complete charging and discharging process of the $S_{9.3}I$ material, only the I^- absorption peak was detected, indicating the existence of a reversible I^0 and I^- conversion reaction. However, the SI material not only has an absorption peak of I^-, but also an absorption peak of I_3^- at 1.2 V during the discharge process. It is notable that the absorption peak of I_3^- disappears during the charging process, indicating that the dissociation of the Zn–S bond during the charging process is mainly due to the interaction between I^- and the ZnS surface, promoting the rapid conversion of I_3^- to I^-.

To further evaluate the existence form and role of iodine in the

electrode material, the morphology and composition of the S_xI cathode material were analyzed after several cycles at a current density of 1.5 A·g^{-1} (Figs. 5(a)–5(f)). The test results show that sulfur and iodine are still uniformly distributed in S_xI after cycling. The conversion of I^0 and I^- on the surface of the electrode material can directly promote the rapid reversible reaction between sulfur and ZnS. Combined with the ultraviolet–visible test results, it can be obtained that a part of the iodine in the S_xI electrode material undergoes redox reactions and exists in the electrolyte in the form of ions, while the other part of the iodine remains in the electrode material. Based on the detailed analysis of the material structure, kinetics, and thermodynamics, the reaction mechanism of S_xI is speculated as shown in Fig. 5(g). To address the inherent challenges of sluggish kinetics and poor electrical conductivity in sulfur cathode materials during conversion reactions, iodine was introduced to construct S_xI composite cathodes. Firstly, iodine can improve the electrical conductivity of commercial sulfur. Secondly, iodine acts as a redox medium and undergoes conversion reactions between I^0 and I^-, I_3^-. I^- promotes the dissociation of the Zn–S bond, reduces the energy barrier of the conversion reaction, improves the catalytic efficiency, and accelerates the reaction kinetics of sulfur.

4 Conclusions

In summary, we construct a series of S_xI cathode materials with high electrical conductivity and catalytic activity. It was proved that the introduction of iodine disrupted the S_8 structure to form new S–I bonds, constructing an electron transfer pathway in S_xI and improving its electrical conductivity. Compared with commercial sulfur, the $S_{9.3}I$ and SI exhibit high discharge capacities of 370.32 and 220.04 mAh·g^{-1} at a current density of 1.5 A·g^{-1}. Their charge–discharge voltage differences are significantly reduced, being 0.84 V and 0.76 V, respectively. The SI has a pair of redox peaks at 1.32/1.38 V, corresponding to the redox of I^0/I^-. Then, I^- can interact with the surface of ZnS to dissociate the Zn–S bond, and some I^- may also be converted into I_3^-, improving the reversibility of cycle. S_xI shows a relatively low Tafel slope value in the redox reaction, indicating that iodine can accelerate the transport of Zn^{2+} and promote the activation of ZnS, exhibiting high catalytic activity. The activation energy of commercial sulfur is 47.69 kJ·mol^{-1}, while the activation energies of $S_{9.3}I$ and SI significantly decrease to 31.87 and 28.48 kJ·mol^{-1}, indicating that iodine reduces the energy barrier of the conversion reaction and improves the catalytic efficiency. The dissociation of the Zn–S bond during the charging process is mainly due to the interaction between I^- and the ZnS surface, promoting the rapid conversion of I_3^- to I^-. This work will promote the application and development of conversion materials in the field of energy storage technology.

Electronic Supplementary Material: Supplementary material (SEM images, electrochemical performance, and the information of DFT) is available in the online version of this article at https://doi.org/10.26599/NR.2025.94908050.

Data availability

All data needed to support the conclusions in the paper are presented in the manuscript and the Electronic Supplementary Material. Additional data related to this paper may be requested from the corresponding author upon request.

Acknowledgements

This work was supported by the National Natural Science Foundation of China (Nos. 22269024 and 62204054), the Key Research and Development Program of Shaanxi Province (No. 2024GX-YBXM-439), and the Shaanxi Province Training Program of Innovation and Entrepreneurship for Under-graduates (No. S202410719123).

Declaration of competing interest

All the contributing authors report no conflict of interests in this work.

Author contribution statement

Q. H. Z.: Writing – original draft, experimental design, methodology, data curation. W. L. Z.: Writing – original draft, conceptualization, software. H. W., C. H. X., R. L., L. X., and X. Y. W.: Investigation, data curation. J. H. B.: Conceptualization, formal analysis. J. W. W.: Writing – review & editing, conceptualization, formal analysis, resources, funding acquisition. F. F.: Conceptualization. All the authors have approved the final manuscript.

Use of AI statement

None.

References

[1] Patel, D.; Sharma, A. K. Minireview on aqueous zinc–sulfur batteries: Recent advances and future perspectives. *Energy Fuels* **2023**, *37*, 10897–10914.

[2] Xu, H. T.; Yang, W. Y.; Li, M.; Liu, H. B.; Gong, S. Q.; Zhao, F.; Li, C. L.; Qi, J. J.; Wang, H. H.; Peng, W. C. et al. Advances in aqueous zinc ion batteries based on conversion mechanism: Challenges, strategies, and prospects. *Small* **2024**, *20*, 2310972.

[3] Nie, X. Y.; Miao, L. C.; Yuan, W. T.; Ma, G. Q.; Di, S. L.; Wang, Y. Y.; Shen, S. G.; Zhang, N. Cholinium cations enable highly compact and dendrite-free Zn metal anodes in aqueous electrolytes. *Adv. Funct. Mater.* **2022**, *32*, 2203905.

[4] Wang, X.; Liu, L. Y.; Hu, Z. W.; Peng, C. C.; Han, C.; Li, W. J. High energy density aqueous zinc–chalcogen (S, Se, Te) batteries: Recent progress, challenges, and perspective. *Adv. Energy Mater.* **2023**, *13*, 2302927.

[5] Chen, J. J.; Xiong, J. M.; Ye, M. H.; Wen, Z. P.; Zhang, Y. F.; Tang, Y. C.; Liu, X. Q.; Li, C. C. Suppression of hydrogen evolution reaction by modulating the surface redox potential toward long-life zinc metal anodes. *Adv. Funct. Mater.* **2024**, *34*, 2312564.

[6] Gao, N.; Cui, M. Y.; Xi, K.; Deng, T.; Yin, D. D.; He, J. J.; Cui, X. F.; Liu, L. M.; Li, W. P.; Ding, S. J. et al. Elimination of concentration polarization under ultra-high current density zinc deposition by nanofluid self-driven ion enrichment. *Adv. Mater.* **2025**, *37*, 2419034.

[7] Wang, K. N.; Wu, D. X.; Sun, X. L.; Zhang, W. L.; Zhang, Z. Z.; Zhen, Y. Z.; Yang, Y. D.; Wang, J. W. Coupling oxygen vacancies and heterophase homostructure achieving high-rate-endurable aqueous zinc-ion storage. *ACS Sustainable Chem. Eng.* **2023**, *11*, 15818–15825.

[8] Wang, J. W.; Wang, H.; Wang, K. N.; Wang, W. H.; Zhang, W. L.; Zhen, Y. Z. Dual modulation of homogeneous nanomaterialization and electrochemical activation enhancing zinc ion storage. *Sci. China Chem.* **2025**, *68*, 385–393.

[9] Zeng, Y. X.; Lu, X. F.; Zhang, S. L.; Luan, D. Y.; Li, S.; Lou, X. W.

Construction of Co–Mn Prussian blue analog hollow spheres for efficient aqueous Zn-ion batteries. *Angew. Chem., Int. Ed.* **2021**, *60*, 22189–22194.

[10] Feng, C. L.; Jiang, X. Y.; Zhou, Q. P.; Li, T. S.; Zhao, Y. F.; Niu, Z. J.; Wu, Y. C.; Zhou, H.; Wang, M. Y.; Zhang, X. C. et al. Recent advances in aqueous zinc–sulfur batteries: Overcoming challenges for sustainable energy storage. *J. Mater. Chem. A* **2023**, *11*, 18029–18045.

[11] Zhang, H.; Yang, M.; Xiao, J.; Wu, Z. B.; Xin, W. L.; Xiao, X. L.; Niu, M. F.; Yan, Z. C.; Zhu, Z. Q. Internal electron donor accelerated sulfur redox for aqueous Zn–S batteries. *Adv. Funct. Mater.* **2024**, *34*, 2406125.

[12] Yan, D.; Yang, H. Y.; Bai, Y. Tactics to optimize conversion-type metal fluoride/sulfide/oxide cathodes toward advanced lithium metal batteries. *Nano Res.* **2023**, *16*, 8173–8190.

[13] Kang, J. M.; Zhao, Z. D.; Li, H. J.; Meng, Y. H.; Hu, B.; Lu, H. B. An overview of aqueous zinc-ion batteries based on conversion-type cathodes. *Energy Mater.* **2022**, *2*, 200009.

[14] Cao, Y. N.; Ju, S. D.; Zhang, Q.; Gao, K.; Marcelli, A.; Zhang, Z. P. Recent progress in aqueous zinc-ion batteries based on conversion-type cathodes. *Adv. Powder Mater.* **2025**, *4*, 100278.

[15] Liu, X.; Li, Y.; Zhou, L.; Mai, L. Q. Rechargeable metal (Li, Na, Mg, Al)–sulfur batteries: Materials and advances. *J. Energy Chem.* **2021**, *61*, 104–134.

[16] Patel, D.; Dharmesh, A.; Sharma, Y.; Rani, P.; Sharma, A. K. Hybrid electrolyte with biomass-derived carbon host for high-performance aqueous Zn–S battery. *Chem. Eng. J.* **2024**, *479*, 147722.

[17] Xu, L.; Wang, W. H.; Wang, H.; Zhang, Z. Z.; Li, Y. P.; Wang, J. W.; Fu, F.; Xu, B. Pitch-derived multifunctional carbon and bimetallic sulfide composite electrodes for aqueous energy storage. *J. Alloy. Compd.* **2025**, *1010*, 177957.

[18] Wang, K. N.; Wang, J. W.; Zhang, Z. Q.; Zhang, W. L.; Fu, F.; Du, Y. P. Pitch-derived 3D amorphous carbon encapsulated sulfur-rich cathode for aqueous Zn–S batteries. *Sci. China Chem.* **2023**, *66*, 2711–2718.

[19] Zhang, W. W.; Wang, M. L.; Ma, J. K.; Zhang, H.; Fu, L.; Song, B.; Lu, S. T.; Lu, K. Bidirectional atomic iron catalysis of sulfur redox conversion in high-energy flexible Zn–S battery. *Adv. Funct. Mater.* **2023**, *33*, 2210899.

[20] Zong, W.; Li, J. T.; Zhang, C. Y.; Dai, Y. H.; Ouyang, Y.; Zhang, L. Q.; Li, J. W.; Zhang, W.; Chen, R. W.; Dong, H. B. et al. Dynamical Janus interface design for reversible and fast-charging zinc-iodine battery under extreme operating conditions. *J. Am. Chem. Soc.* **2024**, *146*, 21377–21388.

[21] Li, W.; Wang, K. L.; Jiang, K. A low cost aqueous Zn–S battery realizing ultrahigh energy density. *Adv. Sci.* **2020**, *7*, 2000761.

[22] Mehta, S.; Kaur, S.; Singh, M.; Kumar, M.; Kumar, K.; Meena, S. K.; Nagaiah, T. C. Unleashing ultrahigh capacity and lasting stability: Aqueous zinc-sulfur batteries. *Adv. Energy Mater.* **2024**, *14*, 2401515.

[23] Zhao, H. Y.; Yin, D. D.; Qin, Y. Y.; Cui, X. F.; Feng, J.; Zhang, Y. N.; Zhao, L. Y.; Gao, N.; Cui, M. Y.; Xiao, C. H. et al. Highly electrically conductive polyiodide ionic liquid cathode for high-capacity dual-plating zinc-iodine batteries. *J. Am. Chem. Soc.* **2024**, *146*, 6744–6752.

[24] Wang, R.; Liu, Y. Y.; Luo, Q. Q.; Xiong, P.; Xie, X. D.; Zhou, K.; Zhang, W. J.; Zhang, L.; Fan, H. J.; Zhang, C. F. Remolding the interface stability for practical aqueous Zn/I_2 batteries via sulfonic acid‐rich electrolyte and separator design. *Adv. Mater.* **2025**, *37*, 2419502.

[25] Zhang, L. J.; Ren, Y.; Liu, X. R.; Han, F.; Evans-Lutterodt, K.; Wang, H. Y.; He, Y. L.; Wang, J. L.; Zhao, Y.; Yang, W. G. Chain breakage in the supercooled liquid–liquid transition and re-entry of the λ-transition in sulfur. *Sci. Rep.* **2018**, *8*, 4558.

[26] Zeng, S. B.; Li, L. G.; Yu, J. P.; Wang, N.; Chen, S. W. Highly crosslinked organosulfur copolymer nanosheets with abundant mesopores as cathode materials for efficient lithium–sulfur batteries. *Electrochim. Acta* **2018**, *263*, 53–59.

[27] Prabhudessai, A. G.; Balaji, S.; Biswas, K.; Dasgupta, R.; Sarkar, P.; Annapurna, K. Correlation between Raman spectroscopy and mechanical properties of As–Sb–S–I chalcogenide glasses. *J. Non-Cryst. Solids* **2019**, *507*, 56–65.

[28] Zhou, J. B.; Chandrappa, M. L. H.; Tan, S.; Wang, S.; Wu, C. S.; Nguyen, H.; Wang, C. H.; Liu, H. D.; Yu, S. C.; Miller, Q. R. S. et al. Healable and conductive sulfur iodide for solid-state Li–S batteries. *Nature* **2024**, *627*, 301–305.

[29] Hei, P.; Sai, Y.; Liu, C.; Li, W. J.; Wang, J.; Sun, X. Q.; Song, Y.; Liu, X. X. Facilitating the electrochemical oxidation of ZnS through iodide catalysis for aqueous zinc-sulfur batteries. *Angew. Chem., Int. Ed.* **2024**, *63*, e202316082.

[30] Wu, W. L.; Wang, S. B.; Lin, L.; Shi, H. Y.; Sun, X. Q. A dual-mediator for a sulfur cathode approaching theoretical capacity with low overpotential in aqueous Zn–S batteries. *Energy Environ. Sci.* **2023**, *16*, 4326–4333.

[31] Zhang, T. S.; Chen, Q. R.; Li, X. R.; Liu, J. H.; Zhou, W. H.; Wang, B. Y.; Zhao, Z. W.; Li, W.; Chao, D. L.; Zhao, D. Y. Redox mediator chemistry regulated aqueous batteries: Insights into mechanisms and prospects. *CCS Chem.* **2022**, *4*, 2874–2887.

[32] Cui, M. W.; Ma, N. G.; Lei, H.; Liu, Y. F.; Ling, W.; Chen, S.; Wang, J. Q.; Li, H. F.; Li, Z. H.; Fan, J. et al. I_3^-/I^- redox reaction-mediated organic zinc-air batteries with accelerated kinetics and long shelf lives. *Angew. Chem., Int. Ed.* **2023**, *62*, e202303845.

[33] Li, Y. Z.; Xu, C. X.; Li, D. M.; Zhang, Y. J.; Liu, B.; Huo, P. P. ZnS/MoS_2 heterostructures on MXene: A strategy for improved polysulfide adsorption and conversion in Li–S batteries. *Chem. Eng. J.* **2024**, *502*, 158151.

[34] Zhu, Y.; Wang, S.; Chen, Y. X.; Zhang, Y. Y.; Feng, Y. F.; Zhang, G. Q. Screened d-p orbital hybridization in turing structure of confined nickel for sulfion oxidation accelerated hydrogen production. *Angew. Chem., Int. Ed.* **2025**, *64*, e202419572.

[35] Jiang, H. L.; Chu, F. Y.; Li, X. C.; Zhao, B.; He, G. H. Constructing highly active sulfur atoms on MoS_2 surface via p–p orbital covalent coupling matching the liquid–solid transition in lithium–sulfur batteries. *Energy Storage Mater.* **2025**, *77*, 104203.

[36] Zhu, Y. R.; Zhao, R.; Xu, Y. T.; Chen, W. H.; Hu, Z. L.; Xi, L. J.; Xie, Y. J.; Hou, H. S.; Liu, T. C.; Amine, K. et al. Anion vacancies coupling with heterostructures enable advanced aerogel cathode for ultrafast aqueous zinc-ion storage. *Adv. Mater.* **2025**, *37*, 2419582.

[37] Guo, Y. F.; Zhu, X. Q.; Zhang, J.; Zhang, T.; Wang, Z. L.; Shan, M. H.; Wang, F.; Cao, C. Y.; Xu, G. Y.; Zhu, M. F. Engineering electrolyte network structure for improved kinetics and dendrite suppression in Zn–S batteries. *Angew. Chem., Int. Ed.* **2025**, *64*, e202422047.

[38] Li, Y. X.; Jia, H. F.; Hao, Y. H.; Ali, U.; Liu, B. Q.; Zhang, L. Y.; Li, L.; Lian, R. Q.; Wang, C. G. Multi-site high-entropy immobilizer for all-iodine species fixation in high-performance zinc-iodine batteries. *Adv. Funct. Mater.* **2025**, *35*, 2419821.

[39] Zhang, P. F.; Li, J. H.; Zhang, S. J.; Li, D. C.; Zeng, S. Y.; Xu, S. L.; Yao, Q. X.; Liu, L. Y.; Ding, L.; Li, H. X. et al. Toward shuttle-free Zn–I_2 battery: Anchoring and catalyzing iodine conversion by high-density P-doping sites in carbon host. *Adv. Funct. Mater.* **2024**, *34*, 2306359.

[40] Yin, D. D.; Li, B. Y.; Zhao, L. Y.; Gao, N.; Zhang, Y. N.; Feng, J.; Cui, X. F.; Xiao, C. H.; Su, Y. Q.; Xi, K. et al. Polymeric iodine transport layer enabled high areal capacity dual plating zinc-iodine battery. *Angew. Chem., Int. Ed.* **2025**, *64*, e202418069.